2023 IEEE International Conference on Robotics and Automation (ICRA 2023)
May 29 - June 2, 2023. London, UK

Towards a Finned-Swimming Exoskeleton: A Robotic Flutter Kicking Testbed and its Corresponding Thrust Generation

Beau P. Johnson, *Student Member, IEEE*, Michael Goldfarb, *Member, IEEE*

Abstract— **While lower limb exoskeletons for above-ground locomotion have been emerging, few attempts have been made to develop an exoskeleton to augment human swimming. Such efforts are hindered by a lack of knowledge surrounding the kinematics and kinetics of human swimming. This paper presents the design of a robotic platform to be used as a finned swimming testbed; describes a controller to generate finned swimming movement; and presents experiments and associated experimental results conducted to explore thrust production resulting from a flutter kick swimming motion.**

I. Introduction

Although a number of lower limb exoskeletons have been developed for purposes of augmenting human legged locomotion [1], few if any have been developed to augment human swimming. Numerous studies have been performed that characterize the movement kinematics and kinetics (i.e., joint torque, speed, and power requirements) associated with human walking and running (e.g., [2]), and this data has been made widely available (e.g., [3]). These studies have been greatly aided, and largely enabled, by the availability of camera-based motion-capture systems used in conjunction with force plates and model-based inverse dynamics computations. Such information is immensely useful and arguably essential when designing an exoskeleton to assist or augment human movement during walking or running.

Unfortunately, few if any similar studies exist for human finned swimming. Among the reasons, it is more challenging to employ underwater motion capture instrumentation and associated markers. In addition to the challenges of recording kinematic data, an even more significant barrier is obtaining kinetic data associated with underwater movement. In the case of walking or running, external forces are relatively easily measured at singular points of contact (i.e., between each foot and the ground) via force plates, and dynamic models entail fairly well-known inertial and gravitational forces. In the case of swimming, environmental forces (i.e., between the water and human) are highly distributed and not reasonably measurable. Further, even if these forces were measurable, analytical models of the dynamics of a human interacting with a fluid are not well known, and therefore could not be easily employed to compute joint torque and power via inverse dynamics, as is common in overground biomechanics. As such, simple data characterizing the biomechanics of human finned swimming are not readily available or measurable.

Some research has been reported towards the development of exoskeletons for human swimming. To date, there have been three efforts (of which the authors are aware) toward the realization of underwater swimming exoskeletons. One such effort described in [4] aimed to augment breaststroke motion with a frog-kick assist device; experiments evaluating the device demonstrated a reduction in the peak electromyography (EMG) signals of the gastrocnemius and soleus while using it. Another research effort explored the conceptual design of several potential concepts for swimming exoskeletons, including ones based on dolphin, sea turtle, and penguin swimming [5]. A third research effort employed a hydraulic actuation system, and has explored modeling, control, and intent recognition associated with a humanoid swimming robot, as described in the review article [6] (but have not otherwise been presented in an archival publication). To date, there has been no demonstration or characterization of the thrust generation capabilities or characteristics of a human-scale, finned bilateral robotic flutter kicking system.

Therefore, in order to start to establish a better understanding of the requirements of a lower limb exoskeleton to augment human finned swimming, the authors have developed a human-scale, bilateral robotic finned swimming test bed, which is intended to be used in underwater experiments to better understand the actuation requirements of such an exoskeleton, and how these relate to thrust generation. This paper describes the design and implementation of this bilateral finned-swimming robotic platform, and reports data from a series of underwater experiments conducted to characterize its thrust generation capabilities.

II. Methods

A. Robotic Testbed Design

A flutter kick is ideally executed with a stiff leg driven primarily by the hip [7]. As such, the robotic system was designed with two actuated hip joints with rigid legs 1 m (39 in) in length, each terminated by a wedge-like foot, onto which a swim fin (ScubaPro Jet Fin) was fitted. To prevent the need for waterproofing mechanical and electrical components, the authors elected to develop an off-board actuation system. Each hip joint is driven by a brushless DC flat motor (Maxon EC90 flat 600W 30V), each mounted to an aluminum frame housing a two-stage chain drive transmission with a reduction ratio of 19.3:1. The second stage of the

Beau P. Johnson is with the Department of Mechanical Engineering, Vanderbilt University, Nashville, TN 37235 USA (corresponding author to provide phone: 615-887-6679; e-mail: beau.p.johnson@vanderbilt.edu).

Michael Goldfarb is with the Departments of Mechanical Engineering and Electrical Engineering, Vanderbilt University, Nashville, TN 37235 (e-mail: michael.goldfarb@vanderbilt.edu).

transmission is mounted on a custom-made dual-spool with a wrap diameter of 44.5 mm (1.75 in) to allow for bidirectional cable actuation in a pull-pull fashion. A 3.2 mm (0.125 in) diameter cable is wrapped around opposing sides of the spool and routed through a 7 mm (0.28 in) Bowden conduit. The cable and conduit terminate at the hip joint, which has a diameter of 89 mm (3.5 in) yielding an additional reduction of 2:1 for a total transmission ratio of approximately 39:1 between the motor and the hip joint. A solid model and fabricated assembly of the motor and transmission are shown in Fig. 1. Assuming an ideal transmission, the cables would be capable of producing a peak torque of approximately 100 Nm and a continuous torque of approximately 60 Nm at each respective hip joint. More realistically, assuming a 65% efficiency of the transmission, the peak and continuous torque at the hip joints would be 65 Nm and 40 Nm, respectively.

A custom embedded system drives the two brushless motors and measures actuator and hip motion for control. The brushless motor control is provided via a microprocessor optimized for signal processing (Microchip DSPIC 33FJ64GS608-E/PT), which communicates via SPI with a 32-bit general-purpose microcontroller (Microchip PIC32 MZ2048EFM100-I/PF), which runs higher level control functions and interfaces with a CAN bus. Incremental position sensing at each motor is calculated using the Hall Effect sensors in each motor, while absolute position sensing at each hip joint is provided by a magnetic position sensor (AMS model no. AS5145H). The system is powered by two four-cell, 6000 mAh lithium polymer batteries (Thunder Power RC 6000 mAh 4S 14.8V ProLite X 25C LiPo) wired in series to achieve a nominal operating voltage of 30 volts.

B. Control

A finite-state-based torque controller was implemented to drive the flutter kick motion, in a manner assumed to be similar to the way humans drive the corresponding motion. The finite state controller included two states for each leg: 1) a power stroke, characterized by flexion of the hip joint and downward movement of the fin; and 2) a recovery stroke, characterized by extension of the hip joint and upward movement of the fin. Each state employed a constant joint torque, with the level of hip torque corresponding to the level of "effort" a swimmer would use when swimming. The absolute position of each joint was used to direct the state transitions of each joint such that they always moved in opposition (i.e., when the right leg executed a power stroke, the left executed a recovery stroke). This control structure therefore essentially provided an oscillator, whereby the hips oscillated between the two states (power stroke and recovery stroke) based on hip angle threshold conditions in the finite state machine. With this control structure, motion of varying amplitudes and frequency could be achieved by varying either the amplitude of the motion or the torque with which the legs executed the power and recovery strokes. The frequency of motion was not controlled directly, but rather resulted from the parameters of the oscillator (i.e., by the torque levels and position thresholds associated with the state controller). A finite state diagram of the controller is shown in Fig. 2.

Fig. 1. A CAD model (left) of one of the two off-board actuation systems and photo of the fabricated equivalent (right).

C. Buoyancy Compensation

During the initial validation of the system, the legs of the device were not neutrally buoyant, and thus required more torque to execute the recovery stroke than the power stroke. To obtain neutral buoyancy, as would be expected in an exoskeletal system, polyethylene foam was affixed to the legs, which allowed the power stroke and recovery stroke to be conducted with a more balanced commanded torque, greatly improving the transient coordination of motion of the legs.

D. Thrust Measurement

In this work, the thrust force generated by the system was calculated with an adaptation of Lighthill's slender body theory and slender body fish model [8-11], which employs a Navier-Stokes model to calculate the thrust and power generated by a slender fish that moves at right angles to the direction of fin motion. According to Lighthill's theory, the flow around a slender body consists of steady flow, (i.e., the swimming speed of the body), and flow due to the transverse motions of the body. To describe the transverse motions of the body, Lighthill defined a cross section, S_x, of the body a distance, x, from the front end along its length, l, and its transverse displacement, $h(x,t)$. This work follows the

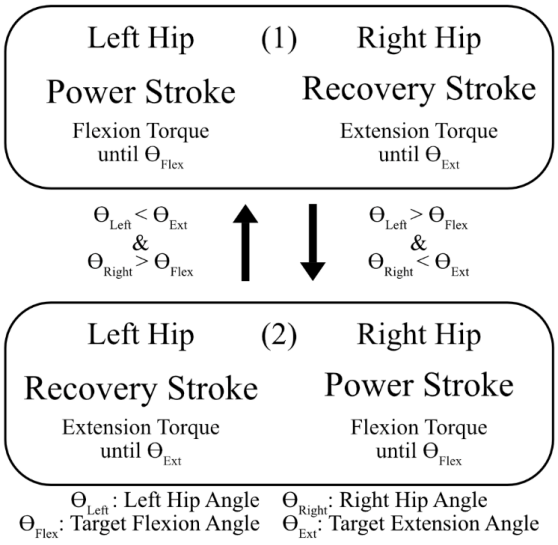

Fig. 2. A finite state diagram of the implemented controller. For each leg, transition conditions are dependent on its position and the position of the opposite leg. Buoyancy compensation aided in the transient coordination of the kicking motion, as the time to conduct the power stroke and recovery stroke was relatively equal. The controller was implemented such that the legs always moved in opposition (i.e. if the left leg being flexed (power stroke), the right leg is extended (recovery stroke), and vice versa).

notation of Lighthill [10] to describe the transverse velocity, *W*, of a given cross-section, and the velocity of a water, *w*, as it sweeps along the body with velocity *U*, as shown.

$$W = \frac{\partial h}{\partial t} \tag{1}$$

$$w = \frac{\partial h}{\partial t} + U\frac{\partial h}{\partial x} \tag{2}$$

By considering the momentum associated with water moving at velocity *w* and the work done by the body moving transversely with velocity *W*, Lighthill derived an equation for instantaneous thrust, *P*:

$$P = [mw\left(W - \tfrac{1}{2}w\right)]_{x=l} - \frac{d}{dt}\int_0^l mw\left(\frac{\partial h}{\partial x}\right)dx \tag{3}$$

Further work by Samimy, Mollendorf, and Pendergast [12, 13] applied this theory to swim fins and demonstrated calculated propulsive thrust forces comparable to those reported by direct measurement [14-16]. Slender body theory may also be used to calculate power and efficiency, but in this work is only used as a validated method for calculation of thrust to verify the ability of the system to produce human-scale thrust. For a more thorough derivation of Lighthill's equations and their application to fin swimming, see [8-13].

E. Thrust Generation Experiments

In order to examine the swimming motion generated by the controller, and to better understand the resulting thrust generation characteristics of the finned swimming platform, experiments were conducted in which the robotic platform was operated underwater in a swimming pool. The experimental setup, along with video frames from the experiments, are shown in Fig. 3. As shown in the figure, the platform was anchored to the side of the pool, with the hip joints affixed to a plate riding on linear bearings and the legs and fins extending into and under the water. The experiments encompass 8 different controller conditions that included two levels of hip torque and four different target motion amplitudes. The four target motion amplitudes were determined by setting thresholds for the target hip flexion and extension angles. The two hip torque levels corresponded to continuous and peak operating conditions of the motors, respectively. In the continuous operating condition (low power), both the power stroke and recovery stroke were conducted at the nominal continuous operating current of the motor, while in the peak operating condition (high power) both were conducted with 1.5 times the motors' continuous current ratings. Each trial was conducted for a duration of 30 s, and each was repeated three times, for a total of twenty four trials.

Fin motion data was captured using two Crosstour Sports Action Cameras, mounted orthogonally to the extended legs. Trials were recorded at 120 frames per second, and analyzed in MATLAB. For each frame, an HSV color thresholder mask was applied to acquire the fin shape. The top edge, bottom edge, and midline were fitted with a polynomial curve to ensure smoothness, and each was used separately to calculate thrust for verification and consistency. Hip kinematics were recorded in MATLAB, and in post-processing the video was field-of-view corrected and synchronized with the data recorded in MATLAB by aligning the timing of onset of motion. The angle and motion of the hip and fin were subsequently calculated by video analysis and verified against the hip angle measured by the absolute encoder. Fin signatures and instantaneous thrust values were calculated for each trial as follows.

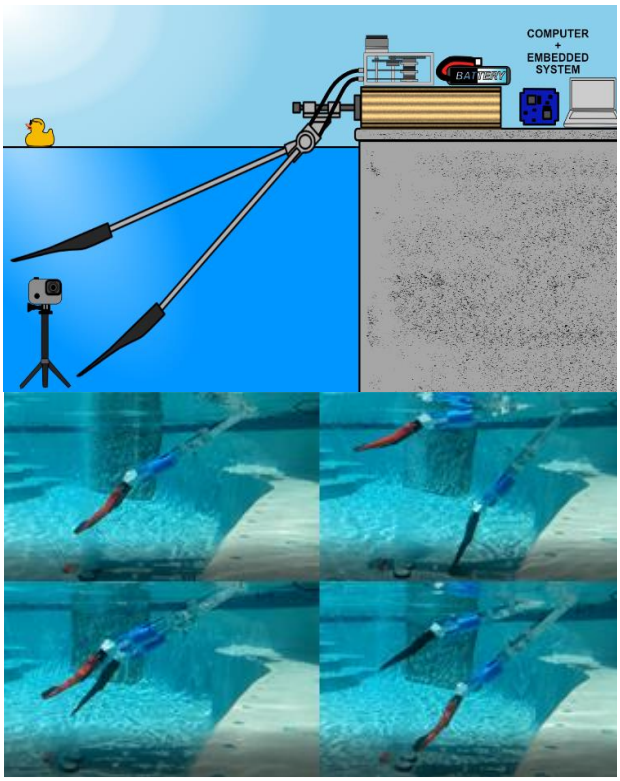

Fig. 3. (a) An illustration of the experimental setup. (b) Still images from the video recording of experimental trials.

In accordance with convention, the foot pocket was excluded from thrust calculations, and thus the leading edge (LE) of the swim fin was taken as the point just behind the foot pocket, and the trailing edge (TE) was taken as the aft portion of the fin. A fin signature [12, 13] was constructed by plotting the path of the LE and TE over time. Applying Lighthill's slender fish model as described above, instantaneous and average thrust were calculated for each trial. Note that in comparable works, fin signatures were constructed by video analysis of swimmers swimming at constant speed, whereas the system herein remained stationary. Thus, in thrust calculations, the free stream velocity, *U,* was considered to be zero, neglecting the effects of the steady flow around the body. A free stream velocity can subsequently be assumed, from which thrust at given speeds can be estimated.

III. RESULTS

A plot of the fin motion, normalized to percent stroke is shown in Fig. 4. Hip angle as measured by the absolute encoder is plotted on the vertical axis, where a hip angle of zero deg is parallel to the surface of the water, and increasing magnitude indicates hip flexion and therefore downward motion of the fin. Strokes were parsed using the initiation of the power stroke, such that zero percent stroke corresponds to

the initial movement of the hip toward flexion (maximum hip extension). Note that the y-axis is inverted, and thus tracing the path from left to right follows the movement of the fin during the stroke. Bolded lines indicate average hip angle for each targeted motion amplitude, and shaded regions indicate one standard deviation from the mean.

In analysis of human swimming, leg motion is often approximated as a sinusoid and characterized by kick depth and frequency. Though position feedback was not utilized in this study, the implemented control algorithm yielded consistent and symmetric kinematics that may be approximated as a sinusoid. In the plots presented below, trials were categorized by amplitude, referring to the peak-to-peak amplitude of motion. Any reference to the amplitude of motion refers to this peak-to-peak amplitude unless otherwise indicated. The frequency of motion achieved, in Hz, is plotted against the amplitude of motion, in degs, in Fig. 5. Note that the frequency and amplitude display an inverse relationship, and a curve fit to this relationship indicates a line of constant power. Specifically, with constant input power, an increase in commanded amplitude will result in a decrease in frequency. The two experimental cases utilized the same torque commands across amplitudes, and thus yield approximately a constant power sweep across motion parameters. Given the relationship shown between frequency and amplitude at a constant power and the utilization of amplitude as a control parameter, plots are shown with amplitude as the dependent variable.

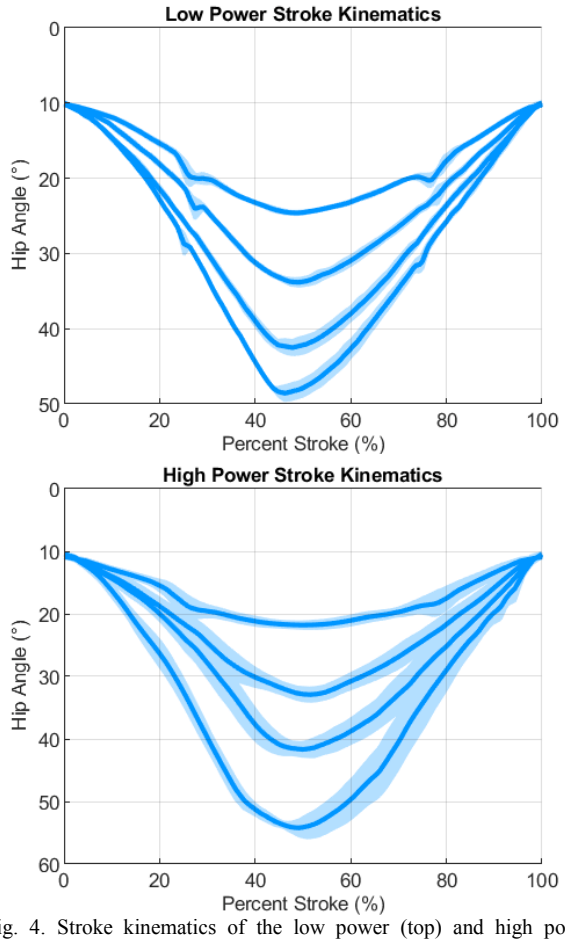

Fig. 4. Stroke kinematics of the low power (top) and high power (bottom) trials. The solid line indicates the averaged hip angle and the shaded region indicates one standard deviation from the mean. Zero percent stroke corresponds to the beginning of the power stroke.

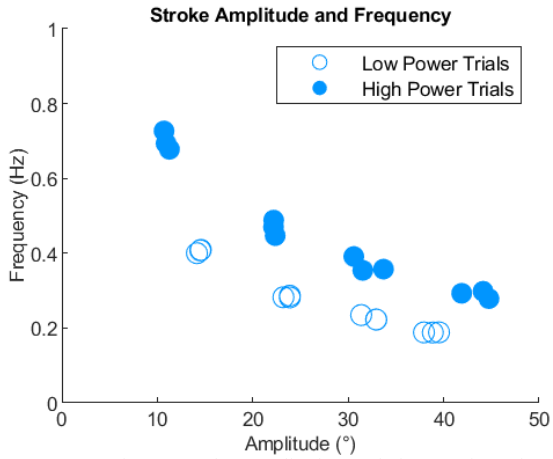

Fig. 5. Approximate stroke amplitudes and frequencies of motion achieved by the testing platform. Note amplitude here refers to the peak-to-peak amplitude of motion, corresponding to twice the amplitude of a sinusoid approximating a given motion.

Note that humans typically modulate their kinematics by changing kick frequency, rather than amplitude. Specifically, kick depth (amplitude) is maintained, and swimming speed is increased or decreased by a corresponding change in kick frequency [17]. While there is certainly some sort of optimization inherent in the control of the human swimming motion, such optimization likely includes factors such as joint range of motion, muscle strength, fatigue, and comfort, which need not be considered as strongly in the optimization of the swimming motion of a robotic system. Further, the reduction of the human kicking motion to a kick depth and frequency neglects the dynamics of the knee and ankle joint. While a fully extended leg is considered optimal for thrust production, it is relatively unachievable by a human swimmer. It is possible that optimal thrust production is achieved by the control of both amplitude and frequency of motion, and thus both were explored in this work- amplitude by control of the target motion amplitude, and frequency by the magnitude of the torque command.

Fin signatures were constructed via video analysis of each trial, and a representative stroke of each motion amplitude and power level is shown in Fig 6. The orientation of the LE of the fin is indicated by the darker line, and the orientation of the TE is shown with a lighter line. Video analysis was conducted at fifteen frames per second, and, for visualization, every other frame was excluded. Thus, each line indicates a time step of 133 ms. Fin signatures for the lower power trials were constructed assuming a steady swimming speed of 0.4 m/s in the direction of the x-axis, and the fin signatures of the higher power trials used a swimming speed of 0.6 m/s.

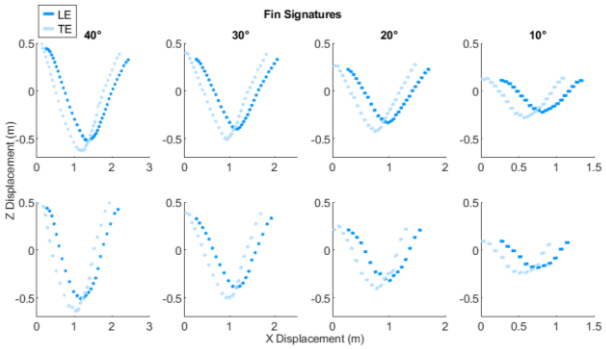

Fig. 6. Fin signatures constructed from video analysis. The direction of forward progression is to the right. The leading edge (LE) of the fin is indicated by the darker solid line and the trailing edge (TE) is indicated by the lighter solid line. For visualization, every other frame was excluded.

Averaged values of instant thrust are plotted against percent stroke in Fig. 7 for each of the motion amplitudes and power levels. The bolded solid line indicates the averaged instant thrust value and the shaded region indicates one standard deviation from the mean. For all trials, instant thrust remained positive except for the transition from recovery stroke to power stroke. The 10 deg amplitude cases yielded the most negative thrust during this transition. The dip in thrust production near 50 percent stroke in each case corresponds to the transition between the power stroke and the recovery stroke. In each case, thrust generation remained positive but was greatly reduced relative to the peak thrust generated during the power and recovery strokes. Peak amplitudes of thrust generated in both the power stroke and recovery stroke increased with motion amplitude. Relative to the low power trials, the high power trials generated greater values of instant thrust, but also demonstrated greater variability in peak magnitude and timing of thrust production.

The mean thrust for each trial is plotted against its corresponding amplitude of motion in Fig. 8. Thrust values shown are twice the mean thrust inferred from the fin

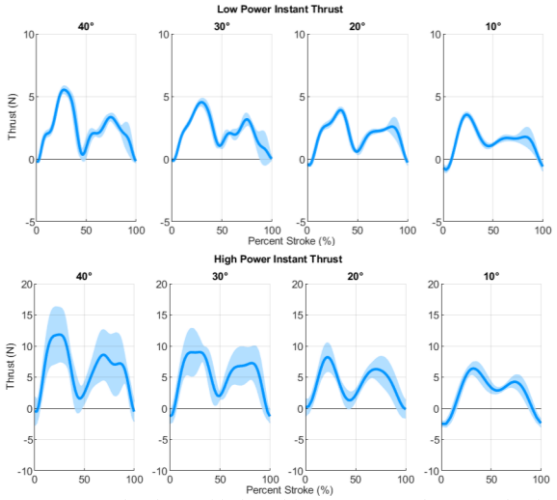

Fig. 7. Averaged values of inferred instantaneous thrust production for low power (top) and high power (bottom) trials. The solid line indicates the averaged values of thrust, and the shaded region indicates one standard deviation from the mean.

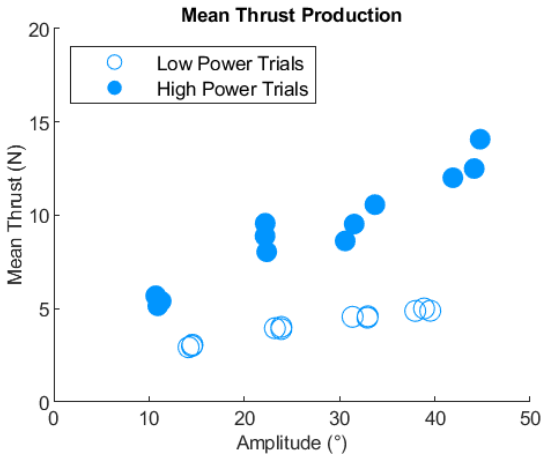

Fig. 8. Mean inferred thrust for each trial plotted against its mean amplitude of motion.

signature of a single fin. In both the low and high power cases, mean thrust production was increased with increased amplitude of motion. For all amplitudes, mean thrust production was approximately doubled in the high-power trials compared to the low power trials.

All trials in this study were conducted with the system stationary and mounted to the edge of the pool. Thus, for the calculation of thrust production, the contribution of the swimming speed, U, was neglected. For comparison to prior recorded thrust measurements using Lighthill's equations, the thrust was also calculated at varying assumed swimming speeds. Mean thrust production values for each case at swimming speeds up to 0.8 m/s are shown in Fig. 9. Solid, blue lines indicate the high power trials. For all cases mean thrust production decreased with increasing swimming speed, and thus reported thrust values represent the maximum thrust value inferred from a given fin signature. The reduction in thrust generation was most prominent in the high power cases, likely due to increased magnitudes of $\delta h/\delta x$. Also shown are

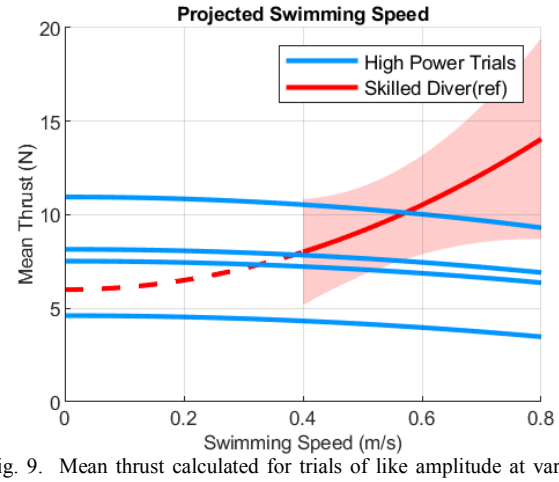

Fig. 9. Mean thrust calculated for trials of like amplitude at varying swimming speeds, U. The highest mean thrust values were observed with the highest motion amplitude and decreased as amplitude decreased. The red line indicates inferred thrust generation of human swimmers swimming at corresponding speeds. The solid line indicates the average thrust generation, the shaded region indicates a fit to the reported standard deviation at each speed, and the dashed line is a projection of the average thrust production to other speeds.

mean thrust values inferred from fin signatures of skilled divers at speeds from 0.4 to 0.8 m/s reported in [13]. The solid line is a polynomial fit to the reported mean values, with a dashed line indicating a projection of this fit as a function of swimming speed, and the shaded region shows a polynomial fit to reported standard deviations.

IV. Discussion

The implemented controller was capable of producing a consistent and coordinated flutter kick motion with both legs at four different motion amplitudes and two commanded torque levels. For a given torque level, the frequency and amplitude of motion displayed an inverse relationship. Specifically, an increase in motion amplitude yielded a corresponding decrease in frequency of motion. The drag experienced by the fin as it moves through the water is proportional to the velocity squared, and thus the power of a given motion is proportional to the velocity cubed, which in turn is a function of the sinusoidal amplitude (half of the peak-to-peak amplitude) and frequency of the motion. Thus, power is proportional to the product of the sinusoidal amplitude and frequency of the motion cubed, and the motions achieved in this study support such a relationship.

Human swimming motions are also often described by a kick depth (amplitude) and frequency. However, rather than change both amplitude and frequency of motion, human swimmers typically maintain a constant kick depth, and modulate kick frequency to control swimming speed. Thus, the modulation of amplitude at a constant power differs from the human control of the swimming stroke. However, the primary difference between the system and a human is the impact of the knee and ankle joints. The optimal swimming stroke for thrust production is executed with an extended knee and ankle. A human must expend metabolic energy to hold an isometric contraction and maintain this knee and ankle configuration throughout the stroke, whereas the system achieves this passively with rigid links between the hip joint and the fin. Thus, the motion of the system and its projected fin signature may be considered ideal. The effects of this can be noted in increased thrust production for a given motion, and limited periods of negative thrust. Though the frequency of motion achieved by the system is somewhat lower than that typically observed in humans swimming with similar amplitudes of motion, the thrust values inferred from the fin signatures in this study are commensurate with values reported by analysis of human swimming at higher kick frequencies.

In this study, mean thrust production was found to increase with stroke amplitude. In general, larger, slower kicks are regarded as superior to smaller, faster kicks for thrust production. However, increasing kick amplitude also increases drag. Centering the stroke motion along the midline of the body limits the increase in drag profile associated with a larger kick, but this may be difficult for a human swimmer as range of motion in hip extension is often limited relative to hip flexion. Further, maintaining an extended knee and ankle may also be more difficult when moving further from a neutral hip. A robotic swimmer might circumvent these issues and operate at motion amplitudes greater than those typically observed in human swimming, though there likely still exists a point of inflection past which increasing amplitude will not increase thrust production.

The experiments described in this work were conducted while the system was held stationary, but the formulation of Lighthill's equations allows for a projection of thrust production at varying swimming speeds. For all trials, increasing swimming speed decreased the thrust inferred, with the high power trials displaying a larger reduction in thrust production. Using data from [13] as a reference, the thrust signatures suggest the fin motion achieved in this work could provide sufficient thrust to achieve a swimming speed of 0.4 to 0.6 m/s.

V. Conclusion

The design of a robotic testbed to emulate the flutter kick swimming motion was presented and a series of experiments was conducted to evaluate its motion and thrust capabilities. A controller consisting of a constant-torque oscillator was found to yield sinusoidal motion and generate human-scale levels of thrust. Relative to the motion characteristics observed in human swimmers, the system operated at slower kick frequencies, but produced thrust comparable to the values reported in human finned swimming. Thrust production was found to increase with increasing motion amplitude, though there likely exists a point at which continuing to increase motion amplitude ceases to increase thrust production. This work constitutes the first empirically reported metrics of the thrust production capabilities of a robotic flutter-kicking swimmer. Future work will measure the power requirements of motion and thrust production to serve as a reference for the design of similar devices and exoskeletons to augment human swimming.

REFERENCES

[1] A. J. Young and D. P. Ferris, "State of the Art and Future Directions for Lower Limb Robotic Exoskeletons," *IEEE Transactions on Neural Systems and Rehabilitation Engineering*, vol. 25, no. 2, pp. 171-182, Feb. 2017.

[2] D. A. Winter, "Biomechanics and motor control of human gait: Normal elderly and pathological,"1991.

[3] J. Camargo, A. Ramanathan, W. Flanagan and A. Young, "A comprehensive open-source dataset of lower limb biomechanics in multiple conditions of stairs ramps and level-ground ambulation and transitions," *J. Biomech.*, vol. 119, Apr. 2021.

[4] Q. Wang *et al*., "An Underwater Lower-Extremity Soft Exoskeleton for Breaststroke Assistance," *IEEE Transactions on Medical Robotics and Bionics*, vol. 2, no. 3, pp. 447-462, Aug. 2020.

[5] P. D. Neuhaus, M. O. O'Sullivan, D. Eaton, J. Carff and J. E. Pratt, "Concept designs for underwater swimming exoskeletons," *IEEE International Conference on Robotics and Automation, 2004. Proceedings. ICRA '04. 2004*, 2004, pp. 4893-4898 Vol.5.

[6] H. Xia, M. A. Khan, Z. Li and M. Zhou, "Wearable Robots for Human Underwater Movement Ability Enhancement: A Survey," in *IEEE/CAA Journal of Automatica Sinica*, vol. 9, no. 6, pp. 967-977, June 2022.

[7] M. Wojtków, & A. Nikodem, (2017). "Biomechanics of diving: the influence of the swimming speed on the kinematics of lower limbs of professional divers," *Acta of bioengineering and biomechanics*, vol *19*, no. 4, pp 117-125, 2017.

[8] M. J. Lighthill, "Note on the swimming of slender fish," *J. Fluid Mech.*, vol. 9, pp. 305-317, 1960.

[9] M. J. Lighthill, "Hydromechanics of aquatic animal propulsion," Ann. Rev. Fluid. Mech., vol. 1, pp. 413-466, 1969.

[10] M. J. Lighthill, "Aquatic animal propulsion of high hydromechanical efficiency," *J. Fluid Mech.*, vol. 44, pp. 265-301, 1970.

[11] M. J. Lighthill, "Large-amplitude elongated-body theory of fish locomotion," *Proc. R. Soc. Lond. B*, vol. 179, pp. 125-138, 1971.

[12] D.R. Pendergast, J. Mollendorf, C. Logue and S. Samimy, "Evaluation of fins used in underwater swimming," *J. of the Undersea Hyperbaric Medical society*, vol. 30, no. 1, 2003, pp. 57-73.

[13] S. Samimy, J. C. Mollendorf and D. R. Pendergast, "A theoretical and experimental analysis of diver technique in underwater fin swimming," *Sports Engineering*, vol. 8, no. 1, pp. 27-38, 2005.

[14] R. A. Christianson, G. Weltman, and G. Egstrom, "Thrust forces in underwater swimming," *Human factors*, vol. *7,* no 6, pp. 561-568, 1965.

[15] G. Minak "Evaluation of the performances of free-diving fins," *Sports Engineering*, vol. *7* no. 3, pp 153-158, 2004.

[16] P. Bardis and D. S. Mathioulakis, "Performance Evaluation of Swim Fins Under Zero Translation Speed," *International Journal of Sports Science & Coaching*, vol. 6 no. 2, pp. 253-268, 2011.

[17] P. Zamparo, D.R. Pendergast, B. Termin and A.E. Minetti, "How fins affect the economy and efficiency of human swimming," *Journal of Experimental Biology*, vol. 205, pp. 2665-2676.